CHEMISTRY OF MATERIALS

Article

pubs.acs.org/cm

Evolution at the Solid Electrolyte/Gold Electrode Interface during Lithium Deposition and Stripping

Lingzi Sang,[†] Richard T. Haasch,[‡] Andrew A. Gewirth,*[,†] and Ralph G. Nuzzo*[,†]

[†]Department of Chemistry and [‡]Frederick Seitz Materials Research Laboratory, University of Illinois at Urbana−Champaign, Urbana, Illinois 61801, United States

Supporting Information

ABSTRACT: Quasi-binary thiophosphate-based solid electrolytes (SEs) are attracting substantial interest for lithium batteries due to their outstanding room temperature ionic conductivities. This work describes reactions occurring at the solid electrolyte (SE)/Au interface during Li deposition and stripping for two exemplary SE materials: β-Li_3PS_4 (β-LPS) and $Li_{10}GeP_2S_{12}$ (LGPS). We used in situ Raman spectroscopy, along with X-ray photoelectron spectroscopy (XPS) and scanning electron microscopy (SEM) to evaluate potential-dependent changes in the chemistry of these materials at active electrode interfaces. For β-LPS, a partially reversible conversion of PS_4^{3-} to $P_2S_6^{4-}$ was found along with the formation of Li_2S during Li deposition and stripping. In contrast, LGPS exhibited only irreversible changes at potentials below 0.7 V vs Li^+/Li. The different behaviors likely relate to differences in the structures of the two SE materials and the availability of easily bridged anion components in close proximity. The work shows that SE integrity at interfaces can be altered by applied potential and illustrates important speciations for the interfacial structures that mediate their electrochemical activities.

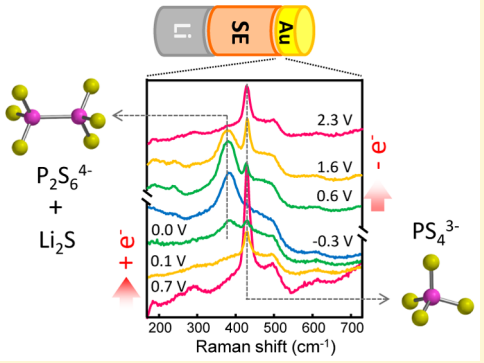

1. INTRODUCTION

Replacing the commonly used liquid electrolyte in lithium ion batteries with a solid electrolyte (SE) has attracted renewed attention over the past few years.[1−18] SE materials have the potential to obviate flammability issues associated with liquid electrolytes, thus increasing battery safety. While early efforts were limited by poor Li^+ conductivity in the SE, this conductivity has dramatically improved over the past decade.[1,7,18,19] Among various types of SE materials, thiophosphate-based SE materials exhibit low grain boundary resistance, high ionic conductivities, and desirable mechanical properties, which makes sintering unnecessary and additionally allows for better SE/electrode interfacial contact.[20,21]

The $Li_{10}GeP_2S_{12}$ (LGPS) SE reported by Kamaya and co-workers[1] exhibits a 1.2×10^{-2} S/cm room temperature Li ion conductivity, which is comparable with that of conventional organic liquid electrolytes. This material exhibits a specific lattice structure composed of GeS_4 and PS_4 tetrahedra which provides multiple Li sites with low energy barriers to Li site hopping.[22] The crystal structure of LGPS is provided in Figure 1A.[1] Kamaya and co-workers attribute the superior conductivity and low transport activation energy to a one-dimensional Li transfer channel on the three Li sites formed from the LiS_6 octahedral and $(Ge_{0.5}P_{0.5})S_4$ tetrahedral substructure that coexists in LGPS.[1] Later, a three-dimensional Li conduction pathway enabled by a fourth interstitial Li site was discovered by NMR spectroscopy[22] and neutron diffraction[23] which is consistent with the most recent predictions from theory.[24−26]

The discovery of LGPS prompted substantial effort to synthesize related materials, such as the recently reported $Li_{9.54}Si_{1.74}P_{1.44}S_{11.7}Cl_{0.3}$.[18] A particularly interesting quasi-binary thiophosphate SE material is β-Li_3PS_4 (β-LPS).[19] The latter compound has the advantage of solution processability, which greatly simplifies SE preparation. Different preparation methods can help stabilize the metastable β phase, which is 3 orders of magnitude more conductive than the crystalline γ form.[19,27,28] The β-LPS polymorph exhibits zigzag arranged PS_4 tetrahedra connected with LiS_6 octahedra via edge sharing.[29] The crystal structure of β-LPS is shown in Figure 1B.

While SE Li^+ conductivity is one area of focus, another issue requiring attention is the nature and evolution of the SE/electrode interface.[18,30,31] Theory suggests that binary thiophosphate-based fast Li conductors present a limited window of thermodynamic stability, a feature suggesting that interfacial chemical reactions may play an important role in their functional behaviors on cycling.[32−34] The reports of large electrochemical windows for SE materials must therefore be a consequence of the formation of passive layers at the electrode/SE interface in analogy to the solid/electrolyte interface (SEI) formed in conventional batteries. Beyond this, many features of the dynamics of ion transport remain unclear. Computational work on LGPS, for example suggests a simultaneous occurrence of PS_4^{3-}/GeS_4^{2-} anion rotation and cation diffusion.[35] Even so,

Received: January 3, 2017
Revised: March 14, 2017
Published: March 14, 2017

DOI: 10.1021/acs.chemmater.7b00034
Chem. Mater. 2017, 29, 3029−3037

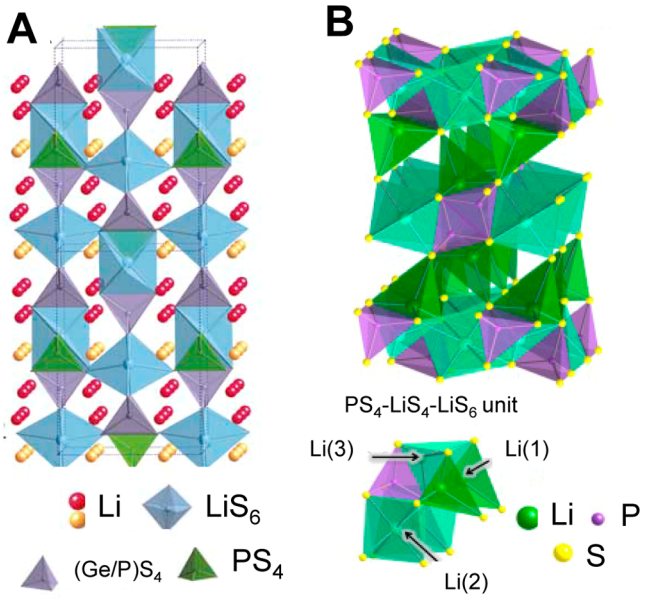

Figure 1. (A) Structure of LGPS. Reprinted by permission of Macmillan Publishers Ltd. (*Nature Materials*) (ref 1), copyright (2011). (B) Structure of β-LPS. Reprinted from ref 29. Copyright (2011), with permission from Elsevier.

Du et al.'s thermodynamic calculations argue that the removal/addition of Li does not alter the structural framework of LGPS.[25]

Experimentally, direct operando observations of active SE/electrode interfaces are still limited. Otoyama and co-workers investigated a cross-sectional $Li_2S-P_2S_5$ glass ceramic/lithium cobalt oxide (LCO) electrode interface after charging and discharging via imaging Raman spectroscopy.[36] Redox reactions of the cathode were observed, and no significant changes were reported for the electrolyte. Wenzel et al. discovered that Li reduces LGPS and forms Li_3P, Li_2S, and a Li–Ge alloy at the LGPS/Li interface once contact to Li metal is made.[37] Similar degradation has also been discovered at the $Li_7P_3S_{11}$/Li interface.[38] There is no equivalent work describing changes that might occur with β-LPS. Additionally, the potential-dependent evolution of the SE/electrode interface is still unclear.

In this work, we performed in situ Raman spectroscopy measurements proximal to the SE/electrode interface in order to evaluate the attributes of its evolution as a function of applied potential. Raman spectroscopy is chosen because of its high structural specificity and extended sensitivity in the low vibrational frequency range, which are ideal for pursuing thiophosphate-related structural information. The LGPS and β-LPS materials are chosen for study as specific exemplars of quasi-binary thiophosphate-based SE materials.

2. EXPERIMENTAL SECTION

2.1. Materials and All Solid Cell Preparation. $Li_{10}GeP_2S_{12}$ (99.5%) (LGPS) was purchased from MSE Supplies LLC (Tucson, AZ, USA) and used without further purification. β-Li_3PS_4 nanoporous solid electrolyte was synthesized as previously reported[19] from Li_2S (99.98% trace metals basis), P_2S_5 (99%), and anhydrous tetrahydrofuran (≥99.9%, inhibitor-free) (all obtained from Sigma-Aldrich Corp). For both β-Li_3PS_4 and LGPS, 0.2 g of powder solid electrolyte material was pressed into a ca. 1 mm thick by 13 mm diameter pellet at 300 MPa in an Ar protected environment. A 50 nm amount of Au was e-beam deposited onto the solid electrolyte (SE) pellet at 0.5 Å/s and served as the working electrode.

2.2. Electrochemistry. A two electrode all solid state electrochemical cell was assembled by placing Li foil (0.75 mm thick, 99.9%; Alfa Aesar) and the SE/Au pellet into a Swagelok cell. Referenced to the Li electrode, the potential of the Au electrode was swept between 2.0 and −0.5 V in β-LPS or 2.0 and −0.1 V in LGPS at a scan rate of 0.2 mV/s. Impedance measurements were performed by using a SP-150 potentiostat/galvanostat (BioLogic Science Instruments). Same measurements were obtained by using blocking electrodes made from Al, following published procedures.[1,19]

2.3. In Situ Raman Cell. The spectro-electrochemical cell designed for in situ Raman spectroscopic measurements at the SE/Au interface is shown in Figure 2. A 50 nm thick Au film served as the working electrode and faced toward the quartz optical window. Au is chosen due to its excellent conductivity, chemical stability, and compatibility with the Raman measurement. A Li strip serving as the counter/reference electrode was pushed against the pristine side of the SE pellet, and the "three layer sample" was compressed against a stub-shaped steel back-contact (ss-contact). A key-shaped steel piece in contact with the Au layer served as a current collector. This cell was made airtight by compressing two ring-shaped silicone gaskets between the quartz window/current collector and current collector/cell body, respectively. Two O-rings around the ss-back contact were set against the cell body to achieve a better seal. The cell was assembled in an Ar filled glovebox prior to measurement.

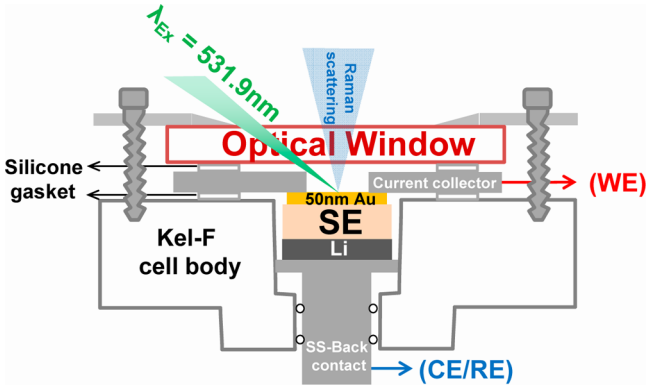

Figure 2. Spectro-electrochemistry cell designed for in situ spectroscopic measurement at solid electrolyte and thin film metal electrode interface.

2.4. Raman Spectroscopy Measurements. A 532 nm laser (B&W Tek Inc.) with a previously described optical arrangement[39] was employed as the excitation source. Raman spectra were collected on a Shamrock SR-303i monochromator (Andor Tech) equipped with a iDus 420 spectroscopy CCD detector (Andor Tech). Spectra in the range of 170–2300 cm^{-1} were acquired. Each spectrum reported in this work was a coaddition of 30 spectra, 2 s integration each.

2.5. X-ray Photoelectron Spectroscopy. XPS measurements were performed on a Kratos Axis ULTRA system (Kratos Analytical) with an Al Kα source at 1486.6 eV and a hybrid spherical capacitor electron energy analyzer. The binding energy was measured relative to the Au $4f_{7/2}$ peak at 84.00 eV in order to eliminate any surface charging effects. The S 2p peak was fitted with a Gaussian line shape in CasaXPS software (Casa Software Ltd.)

3. RESULTS AND DISCUSSION

3.1. Li Deposition and Stripping at SE/Au Interface. We first examine the Li deposition and stripping chemistry on Au via cyclic voltammetry (CV). Panels A and B of Figure 3 show the first two CV cycles at β-LPS/Au and LGPS/Au interfaces, respectively. During the negative sweeps, Li^+ is removed from the electrolyte and deposited onto Au in the

DOI: 10.1021/acs.chemmater.7b00034
Chem. Mater. 2017, 29, 3029–3037

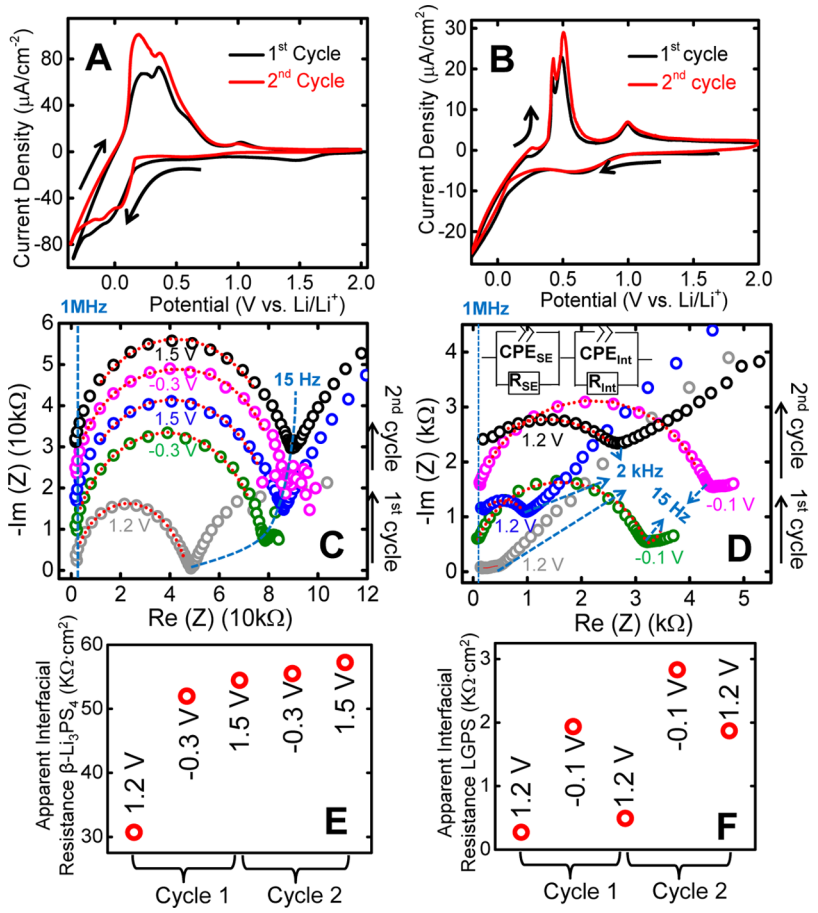

Figure 3. Cyclic voltammograms obtained from (A) Li/β-LPS/Au, (B) Li/LGPS/Au all solid cell with sweep rate of 0.2 mV/s and Nyquist plots of impedance measurements for (C) Li/β-LPS/Au and (D) Li/LGPS/Au cells during the first and second Li deposition and stripping cycles. The impedance plots are stacked with an 7 kΩ offset in panel C and 500 Ω offset in panel D. Apparent interfacial resistance during CV cycles for (E) Li/β-LPS/Au and (F) Li/LGPS/Au.

form of metallic Li and a Au−Li alloy,[40] while during the positive sweep, decomposition of the Au−Li alloy occurs as Li strips from the electrode and reinserts into the electrolyte. The measured CV data using both β-LPS and LGPS are comparable with literature reports.[1,19] We note, however, that the current density is 1 order of magnitude lower relative to that obtained using an equivalent liquid electrolyte system;[41] this difference might be related to differing mobilities of Li between the solid and liquid electrolytes. We also observed cathodic currents during the negative sweeps at potentials slightly above zero. This is due to the underpotential deposition of Li onto the Au electrode.[40] Regardless of the SE material type, the second cycle (red) exhibits a higher stripping current and slightly lower deposition current relative to the first cycle (black). This observation is clearly reflected in the coulombic efficiencies (CE) calculated from these sweeps. β-LPS/Au interface shows a first cycle CE of 28%, while the CE is 74% on the second cycle. For LGPS, CE = 17% and 45% are found for the first and second cycles, respectively. The low CE implies that only part of the Li deposited on the Au electrode is extracted during the anodic sweep. Analogously, previous work reported in situ EQCM measurements that also show the mass loading on a Au electrode is more significant after the first CV cycle compared to the following cycles from 1 M $LiPF_6$ EC:DMC electrolyte, with a noticeable surface morphology change being introduced after Li chemistry resulting from the Au−Li alloy formation and degradation.[41]

Panels C and D of Figure 3 report the Li/SE/Au cell impedance measurement for β-LPS (Figure 3C) and LGPS (Figure 3D) electrolyte during the first two CV cycles. Both Li/SE/Au cells exhibit dramatic changes in the corresponding Nyquist plots as a function of potential. Qualitatively, the Li/β-LPS/Au cell shows a dramatic overall increase in cell resistance following the initial Li deposition process, followed by further slow resistance increases. In contrast, the Li/LGPS/Au system experiences much higher overall cell resistance at lower potentials relative to higher potentials. An appreciable increase in overall cell resistance is observed at both low and high potentials as a function of cycle number.

In order to better define the cell impedance evolution quantitatively, we fit the impedance data to an equivalent circuit shown in the inset to Figure 3D.[37] The equivalent circuit separates the response into two interfacial components: (1) a bulk electrolyte material resistance (R_{SE}) in parallel with a constant phase element (CPE_{SE}) originating from grain boundaries that exist inherently in SE materials and (2) an "apparent interfacial component" (R_{Int} and CPE_{Int} in parallel). The magnitude of the apparent interfacial resistance seen here reflects contributions from all of the interfaces present in the cell including those involved in the Li/SE and SE/Au interactions. In order to fit the equivalent circuit, we obtained

DOI: 10.1021/acs.chemmater.7b00034
Chem. Mater. 2017, 29, 3029−3037

R_{SE} for β-LPS and LGPS from a separate impedance measurement by using a SE pellet placed between two blocking electrodes. The conductivity values obtained for β-LPS and LGPS were 1.0×10^{-4} and 1.0×10^{-2} S/cm, respectively, which are similar to reported values.[1,19] The data fitting parameters as well as Bode plots are provided in the Supporting Information (Figure S1 and Table S1). Notably, the impedance spectrum of LGPS at 1.2 V before the first Li deposition presents two well-resolved resistance components, one of which is associated with the degradation of LGPS when contacting Li.[37] In contrast, β-LPS shows an apparently more robust stability against Li, as we did not observe any additional interface-related components in the impedance spectra measured before Li electrochemical cycling (Figure S2).

With the measured R_{SE} values, the apparent interfacial resistance is extracted by fitting the impedance curves and plotted as a function of cycle history in Figure 3E,F. As expected the Li/β-LPS/Au cell exhibits drastic growth of the interfacial resistance following Li deposition onto Au indicating an interfacial layer with low ionic conductivity must have formed. Alternatively, the Li/LGPS/Au cell exhibits an oscillating pattern where the interfacial resistance is low at positive potentials and high at negative potentials. Prior work reports that the Li/LGPS interface degrades with time,[37] which may be manifested in the apparent progressive increase in the interfacial resistance with cycle number seen in the data presented in Figure 3F. The greater inherent conductivity of LGPS relative to β-LPS may be reflected in the substantially lower interfacial resistance obtained for LGPS relative to β-LPS. Both the CV and impedance results indicate that the two sulfur-based solid electrolytes exhibit marked interfacial chemical/structural evolution upon Li deposition and stripping, the presence of which alters the Coulombic efficiency and cell impedance.

3.2. Potential-Dependent Evolution of the β-LPS Electrolyte at a Au Electrode Surface. In order to investigate the evolution of the electrode/SE interface following deposition and stripping, we measured operando Raman spectra proximate to the Au/SE interface. Figure 4A shows a Raman spectrum obtained from bare β-LPS along with a series of potential-dependent Raman spectra obtained from a Au-covered β-LPS surface. The bare β-LPS spectrum (red) exhibits five vibrational modes, the detailed assignments for which are provided in Table 1. The peaks labeled A, B, and D are deformation modes of S−P−S in PS_4^{3-},[42−45] Peak F is the symmetric stretch of PS_4^{3-}, and peak H at 581 cm^{-1} is the asymmetric PS_4^{3-} stretch.[37,38,42,43] This spectrum is consistent with that previously reported.[19,42]

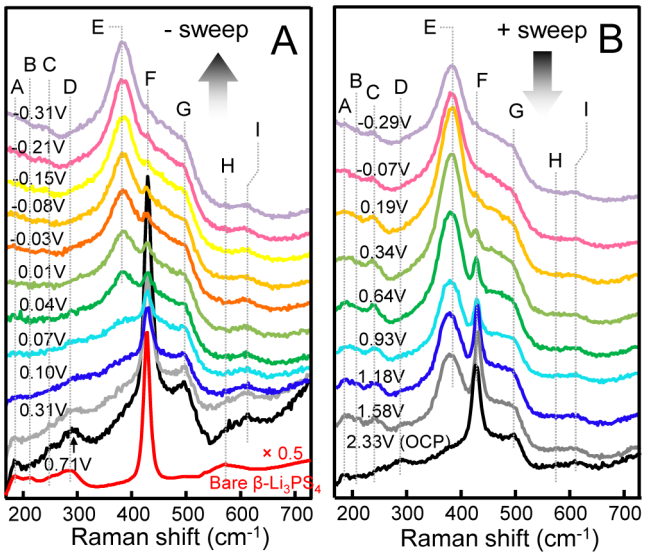

Figure 4. In situ Raman spectra at β-LPS solid electrolyte and 50 nm Au interface during (A) negative and (B) positive potential sweeps.

The Raman spectrum obtained following Au deposition onto β-LPS is similar to the spectrum obtained at 0.709 V (black in Figure 4A). This spectrum shows a new band (G) at 493 cm^{-1}. This peak is assigned to the S−S stretch in Li_2S_x,[46,47] the presence of which suggests that a small amount of material degradation occurs following Au deposition. Additionally, the peak labeled H at 581 cm^{-1} shifts to 607 cm^{-1} (denoted as I) after Au deposition. Peak I is often observed in the Raman spectra of transition metal bridged alkali metal thiophosphates following bidentate sulfur coordination.[43,44,48,49] This observation suggests that Au−S coordination, resulting in lowered symmetry of PS_4^{3-}, may be a consequence of Au deposition onto β-LPS. The Au−S vibration typically appears at 200−300 cm^{-1}[50] which is likely overlapped with peak B or D if it exists, otherwise no other evidence for a Au−S bond was observed. The similarity of the β-LPS spectra before and after Au deposition suggests that β-LPS is not significantly affected by Au deposition. The minor degradation inferred is likely a consequence of the elevated sample temperature occurring during Au deposition.

Also shown in Figure 4 are a series of Raman spectra obtained during the negative (Figure 4A) and positive (Figure 4B) potential sweep of the Li/β-LPS/Au cell. One obvious change seen in the spectra during the negative potential sweep is the progressive increase in the intensity of peak E at 380 cm^{-1} and the corresponding decrease in the intensity of peak F at 426 cm^{-1}. During the positive sweep, peak E decreases in intensity while that of peak F grows back. Peak E is assigned to the symmetric stretch of PS_3 in the "ethane-like" $P_2S_6^{4-}$ moiety.[46,47] The coupled behavior of peaks E and F suggests a conversion of PS_4^{3-} units into a $P_2S_6^{4-}$ dimer at the low potentials accompanying Li^+ reduction to metallic Li and subsequent plating onto the Au electrode surface. To preserve stoichiometry, additional S-containing species (e.g., Li_2S) would also need to form. On the positive sweep, Li^0 to Li^+ oxidation results in at least a partial reversion of the chemistry with a conversion of some $P_2S_6^{4-}$ back to PS_4^{3-}. Other changes in the spectra support this hypothesis. In the S−P−S deformation mode frequency range; peaks A at 179 cm^{-1}, B at 220 cm^{-1}, and D at 426 cm^{-1} diminish during the negative potential sweep and grow back on the positive potential sweep. Similarly, peak C at 238 cm^{-1} grows during the negative sweep and diminishes on the positive one; this behavior is consistent with that of peak E. Although these weak S−P−S deformation modes are not very clearly assigned to specific forms of PS_x, peaks A, B, and D are observed in the Raman spectrum of Li_3PS_4 while peak C is observed in the Raman spectra of $Li_4P_2S_6$.[42]

Figure 5 shows plots of the potential-dependent change in the intensities of peaks E and F. Examples of the peak fitting protocols used to extract these results are provided in Figure S3 and Table S2 in the Supporting Information. The red data points represent the peak intensities seen during negative sweeps; the black data points are taken from the corresponding positive sweep. These data clearly show that the intensity of

DOI: 10.1021/acs.chemmater.7b00034
Chem. Mater. 2017, 29, 3029−3037

Table 1. Vibrational Assignments of β-Li_3PS_4/Au Interface Spectra during Li Deposition and Stripping

	frequency (cm^{-1})				
	β-Li_3PS_4	β-Li_3PS_4/Au (50 nm)			
peak labels	pristine	before cycle	during cycle	assignment	ref
A	179	179		δ_{def}(S−P−S) in PS_4^{3-}, $\delta(PS_4^{3-})$	42−45
B	220		220		
C			238	δ_{def}(S−P−S) in $P_2S_6^{4-}$	42
D	286	286		δ_{def}(S−P−S) in PS_4^{3-}	42−45
E			385	$\nu_s(PS_3)$ and ν(P−P) in $P_2S_6^{4-}$	46,47
F	426	426	426	$\nu_s(PS_4^{3-})$ in PS_4^{3-}	43−47,49
G		493	493	ν(S−S) in Li_2S_x	46,47,52
H	581			ν_{as} (PS_4^{3-}) in PS_4^{3-}, no Au	43,44,49
I		607	607	$\nu_{as}(PS_4^{3-})$ in PS_4^{3-} with Au	43,44,48,49

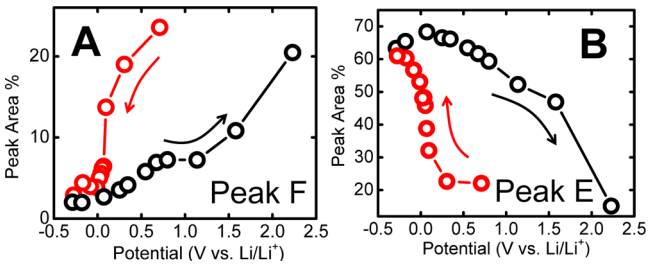

Figure 5. Peak area (%) evolutions of (A) peak F and (B) peak E relative to the entire 320−540 cm^{-1} band envelope as a function of potential. (Examples of peak fitting spectra are shown in Figure S1.).

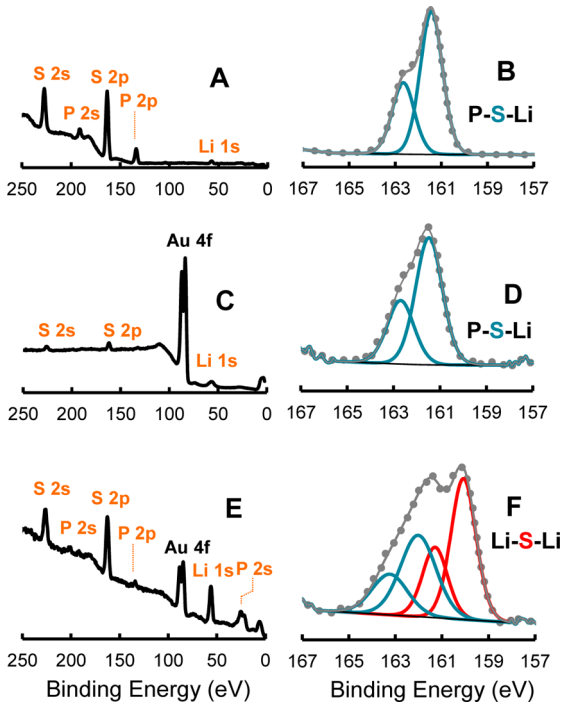

Figure 6. XPS survey (A, C, and E) and S 2p spectra (B, D, and F) of (A and B) bare β-LPS surface, (C and D) β-LPS/Au surface before CV; (E and F) β-LPS/Au surface after CV. S 2p peak assignments are color coded.

vibrational mode F (associated with PS_4^{3-}) decreases during the negative sweep and increases with the positive sweep. Peaks A and D exhibit similar behaviors (Figure S4A,B). In contrast, the mode labeled E (associated with $P_2S_6^{3-}$) as well as peak C (Figure S4C) exhibits the opposite trend. We conclude that PS_4^{3-} degrades during Li^+ removal from the electrolyte, forming in part as a consequence of $P_2S_6^{4-}$, which can reversibly convert to PS_4^{3-} as Li^+ is reintroduced into the SE. As noted above, this interconversion must involve another speciation of sulfur (whether sulfide or polysulfide) to maintain stoichiometric balance. $Li_4P_2S_6$ is known as a poor Li ion conductor[51] (σ_{RT} = 1.6 × 10^{-10} S cm^{-1}), the formation of which is consistent with the growth of interfacial resistance upon cycling observed in Figure 3. The operando Raman data, while consistent with such an inference, does not establish its presence to the same degree (save by inference) as is true for the partner PS_4^{3-} and $P_2S_6^{4-}$ moieties. Other data presented below do affirm the full speciations as described above. We also note that there is hysteresis in these interconversions. This is seen in comparing the series of Raman spectra during Li deposition vs stripping; the forward and backward reactions occur at different potentials. While the PS_4^{3-} to $P_2S_6^{4-}$ conversion occurs promptly with Li deposition, the $P_2S_6^{4-}$ to PS_4^{3-} back-conversion is only complete at 2.3 V.

In order to further investigate the potential-dependent transformations of structure occurring at the β-LPS/Au interface and evaluate the putative presence of irreversibly formed species, we used X-ray photoelectron spectroscopy (XPS). The data in Figure 6 show XPS survey spectra obtained from the bare β-LPS surface (Figure 5A) and the Au-covered β-LPS surface before (Figure 6B) and after (Figure 6C) three CV cycles between 2.3 and −0.5 V in the binding energy range of 0−250 eV. As observed in the XPS survey spectra in Figure 6B, Au deposition covers the β-LPS surface and reduces the S, P, and Li signal intensity. Following the potential sweeps, however, the Au intensity decreases relative to those associated with S, P, and Li. This observation suggests that the structure of Au/β-LPS interface is modified in a significant way during the scans, whether via SE and Li-based materials migrating through the 50 nm thick Au layer or a mechanics-driven coarsening of the Au into a less coherently wetted overlayer. The microscopy data presented below affirm the importance of the latter point. Qualitatively, the Li 1s to the S and P 2p peak ratios are significantly higher after CV cycling as compared to that of the bare β-LPS electrolyte surface. This latter observation supports a preferential migration of Li through the Au during Li deposition. However, unlike the Li deposition and stripping processes from the liquid electrolyte, counterion penetration and reconstruction of the Au electrode are also involved as a likely consequence of the strong and direct Li−anion interactions in the solid/electrolyte materials.

DOI: 10.1021/acs.chemmater.7b00034
Chem. Mater. 2017, 29, 3029−3037

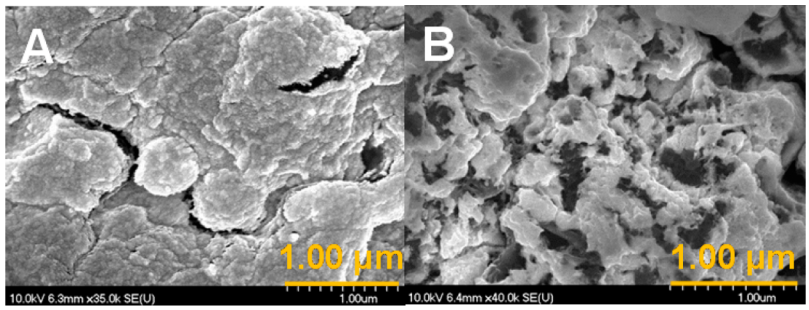

Figure 7. SEM images of 50 nm Au on β-LPS solid electrolyte surface (A) before and (B) after three Li deposition stripping cycles.

Scheme 1. Proposed SE/Au Interface Reaction Mechanism Based on Raman and XPS Results[a]

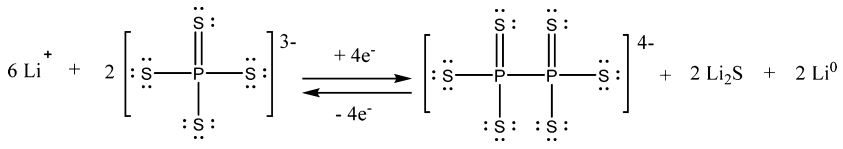

[a]Only one of the PS_4^{3-} and $P_2S_6^{4-}$ resonance structures is shown.

The data in Figure 6 also compare the local electronic environment of the sulfur species at the β-LPS/Au interface as seen before and after CV cycling. Figure 6B shows the S 2p spectra of the bare β-LPS pellet surface along with the Au-covered β-LPS surface before (Figure 6D) and after (Figure 6F) Li deposition and stripping chemistry. We observed only one S 2p component in the XPS spectra before and after Au deposition. The S $2p_{3/2}$ and S $2p_{1/2}$ set near 161.5 eV represent S species in the P−S−Li structure.[37,38] After three cycles of Li deposition and stripping (Figure 6F), we observe a new reduced S 2p component at 160.1 eV which is assigned to S^{2-} in the form of Li_2S.[37,38] This observation strongly affirms the coupled speciations underlying the transformations of SE bonding seen in the operando Raman data of Figure 5. The P−S−Li peak group at 161.5 eV is shifted slightly toward higher binding energy (162.0 eV) suggesting a very slight decrease in electron density which is possibly due to the conversion of a small amount of PS_4^{3-} to $P_2S_6^{4-}$. The XPS peak fitting parameters are tabulated in Table S3 in the Supporting Information.

In order to better understand the changes in morphology occurring at the thin film Au electrode on cycling, we acquired the SEM image at the β-Li_3PS_4/Au surface before (Figure 7A) and after (Figure 7B) CV cycles. Figure 7A shows a uniformly bright surface, consistent with the presence of coherently wetted Au coating. In contrast, Figure 7B shows the presence of a more complex morphology, one highlighting regions of low secondary electron emission. These dark regions are associated with cracks forming in the Au electrode during Li−Au alloy formation and breakdown. We note that significant surface morphology changes are also found on bulk-Au electrodes after Li plating and stripping from liquid electrolyte systems.[40,41]

The XPS and in situ Raman results provide insight into reactions occurring at the SE/Au interface during Li deposition and stripping, as shown in Scheme 1. Here, Li^+ accepts an electron and plates onto the Au electrode in the form of metallic Li. At the same time local Li^+ depletion results in reduction of PS_4^{3-} to form $P_2S_6^{4-}$. Li_2S, seen clearly in the XPS data (Figure 6), accumulates at the β-LPS/Au interface as a consequence of dimer formation. As reported previously, Li_3P (P(III)) is formed as decomposition product of LGPS in contact with metallic Li;[37] the $P_2S_6^{4-}$ (P(IV)) observed here is likely a kinetically controlled product. Upon Li^0 oxidation and reinsertion of Li^+ into the electrolyte, the $P_2S_6^{4-}$ dimer is oxidized to form PS_4^{3-} and Li_2S is consumed. The slow kinetics of PS_4^{3-} reformation, as is seen in the Raman, suggests that one or both of these processes are slow. Additionally, we note that the PS_4^{3-} reformation process is only quasi-reversible, as the PS_4^{3-} intensity does not recover fully in the Raman data, even at 2.3 V. We note that the S 2p local electronic structure change after cycling suggests the partial irreversibility of the monomer formation process as well. Additionally, after three cycles of Li deposition and stripping chemistry, the cell OCP dropped to 1.4 V from the initial 2.3 V, which provides further evidence for the SE/Au interface compositional change. The transformation shown in the scheme illustrates the simplest embodiment of this chemistry, that of a fully reversible conversion of species mediated by a formal 4 e^- transfer process.

3.3. Evolution of $Li_{10}GeP_2S_{12}$ Electrolyte at Au Electrode Surface. We examined the generality of Li coupled structural changes found for β-LPS at the metal/electrolyte interface substituting for it the well-known fast Li^+ conductor LGPS. We first examined the evolution of LGPS at the LGPS/Au interface. Figure 8 shows the Raman spectra obtained from bare LGPS (red) and a series spectra obtained from Au-covered LGPS as a function of applied potential. The spectrum obtained from bare LGPS exhibits six peaks as described previously[42] where assignments are summarized in Table 2. Following Au deposition, a new peak (F′) emerges at 489 cm^{-1} (black spectrum in Figure 7A). As with the β-LPS spectrum described above, this peak is assigned to the S−S stretch in Li_nS_x species resulting from the Au deposition process. The upshift of the asymmetric PS_4^{3-} stretch from 581 to 603 cm^{-1} indicates the existence of Au−S bonding interactions. Peaks A′−E′ and G′ are all signature vibrational modes of the LGPS, as reported previously.[42]

As the applied potential is varied, the LGPS signature peaks A′−E′ all exhibit a very similar trend: a significant decrease in intensity during the negative sweep with hardly any recovery upon the positive sweep. To better illustrate this trend, the relative peak intensities are plotted in Figure 9 as a function of the applied potential. Except for the relatively invariant peak F′

DOI: 10.1021/acs.chemmater.7b00034
Chem. Mater. 2017, 29, 3029−3037

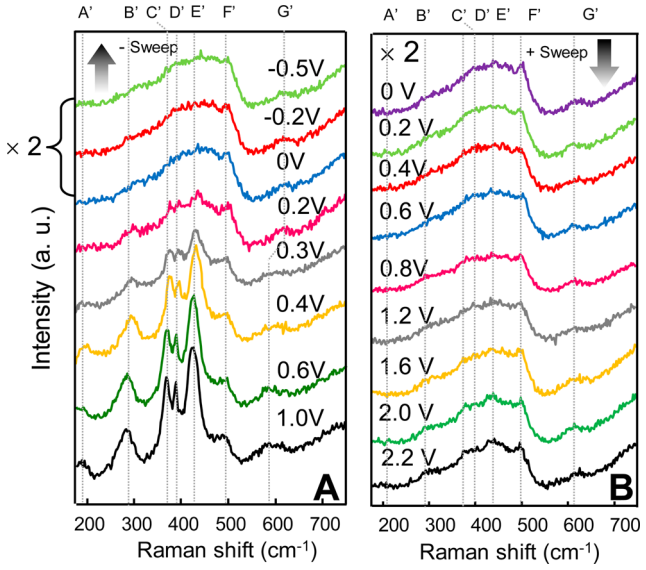

Figure 8. In situ Raman spectra at LGPS/Au interface during (A) negative and (B) positive potential sweep (relative intensities are doubled).

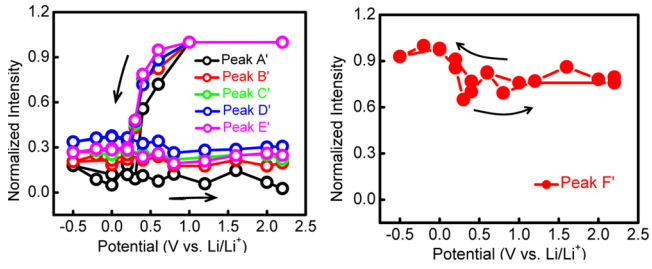

Figure 9. Raman intensity of (A) peaks A′−E′ and (B) peak F′ at the LGPS/Au interface as a function of potential. The intensity of each peak is normalized to its highest intensity during the CV cycle.

shown in Figure 8B associated with Li_2S_x, the intensity of the LGPS signature peaks A′−E′ shown in Figure 8A decrease in intensity starting at 0.7 V on the cathodic scan and reach an intensity minimum at 0.3 V. This potential occurs prior to the potential where substantial Li deposition occurs (ca. 0.1 V) which suggests an electrochemical process for LGPS degradation. This observation is consistent with calculations suggesting a narrow electrochemical window for LGPS stability.[32,33] Figure 8B shows that recovery of the LGPS associated bands does not occur on the positive sweep, suggesting irreversible decomposition.

In contrast to the case shown in Figure 8A, where the cathodic limit was −0.5 V, when the cathodic potential is limited to 0.1 V, partial recoveries of the signature peaks in LGPS were observed at anodic potentials (Figure S5). The intensities plotted as a function of potential are provided in Figure S6 in the Supporting Information. Even more intensity recovery was found when the potential is held at the OCP (2.2 V) for ca. 30 min.

While the spectra presented in Figure. 8B do not exhibit peaks which could clearly demarcate degradation products, we note that the broad 250−520 cm^{-1} band overlaps with the LGPS modes seen initially. Thus, this broad band is likely associated with the presence of various unresolved P−S or S−S structures formed as degradation products.

Previously developed Li transfer mechanisms for LGPS implicate the 3D cross-linked Li transfer channel as the locus of Li ion conductivity.[24,35] Our experimental observation suggests that the Li ion transfer channel in LGPS is not stable at the electrode/electrolyte interface against low potentials and/or Li^+ depletion. Degradation results in accumulation of interfacial products which alter the cell impedance and, by inference, could also impact battery cycle life.[1,32,33]

The two quasi-binary thiophosphate materials studied here share similar PS_4 tetrahedral structural elements yet exhibit very different structures. In the case of β-LPS, Li^+ reduction and plating leads to a quasi-reversible conversion of PS_4^{3-} to $P_2S_6^{4-}$ at the electrode/electrolyte interface. In contrast, LGPS is not as stable and exhibits irreversible changes in its interfacial chemical speciation, particularly below 0.1 V. Experimentally, the $P_2S_6^{4-}$ dimer was not observed at the LGPS/Au interface. The origin of the different behaviors found for LGPS and β-LPS must relate to their different structures. The β-LPS material features tetrahedral PS_4 centers in close proximity (2−3 Å) to each other. As Li is reduced, the dimer forms, and S is extracted to form Li_2S. In contrast, in LGPS PS_4 is in a very different environment, i.e., close to a GeS_4 center. The interfacial products formed at the phase boundary also appear to be determined by the stabilities of the intermediate products. Indeed, DFT calculations suggest that Li_3PS_4 forms $Li_4P_2S_6$ and S at its anodic potential limit while LGPS forms Li_2GeS_3, Li_3PS_4, and S instead.[32]

4. CONCLUSIONS

We used in situ Raman, along with XPS and SEM, to examine the structure and reactivity of two solid electrolytes during Li plating and stripping associated with charge and discharge, respectively. Our results suggest that counterion reconstruction is coupled with Li redox chemistry at the SE/electrode interfaces. Ideally at the liquid electrolyte/electrode interface,

Table 2. Peak Assignments of $Li_{10}GeP_2S_{12}$/Au Interface during Li Deposition and Stripping

peak labels	pristine	with 50 nm of Au before cycle	with 50 nm of Au during cycle	assignment	ref
A′	178	185	185	δ_{def}(S−P−S), $\delta(PS_4^{3-})$	43−45,49,52,53
B′	282	284	284		
C′	368	367	367	$\nu(Li^+-S^-)$	47,54
D′	387	388	388	ν(Ge/PS_4) and $\nu_s(PS_3)$ in $P_2S_6^{4-}$	46,47,55
E′	425	428	428	$P_2S_7^{4-}$ at 410; ν(Ge−S−Ge) with bridging S at 415; PS_4^{3-} at 420	43,44,46,47,55
F′	499	489	489	ν(S−S) in Li_2S_x	46,47
G′	556	580	605	$\nu_{as}(PS_4^{3-})$ in PS_4^{3-} and $P_2S_7^{4-}$	43−45,48,49
	577				

DOI: 10.1021/acs.chemmater.7b00034
Chem. Mater. 2017, 29, 3029−3037

redox active species are (de)solvated and (de)absorbed at the electrode surface during electron transfer process and the counterions remain intact. In contrast, at SE/electrode interface, Li^+ redox and transport processes appear to require breaking and rebuilding of the ionic framework in the SE. In the cases examined here, this process results in counterion transformation which, depending on the specific properties of the materials, may or may not be reversible. Understanding, controlling, and eventually engineering the specific desirable SE/electrode interface is essential for optimizing the performances of all solid Li batteries.

■ ASSOCIATED CONTENT

Supporting Information

The Supporting Information is available free of charge on the ACS Publications website at DOI: 10.1021/acs.chemmater.7b00034.

(Figure S1) Bode plots obtained from the Nyquist plots in Figure 3; (Figure S2) Nyquist plots obtained from impedance measurements; (Figure S3) examples of peak fitting results; (Figure S4) potential dependence of peak intensities; (Figure S5) Raman spectra; (Figure S6) evolution of normalized Raman intensities; (Table S1) interfacial resistance and capacitance during cycles; and (Table S2) peak fitting parameters (PDF)

■ AUTHOR INFORMATION

Corresponding Authors

*(A.A.G.) E-mail: agewirth@illinois.edu.
*(R.G.N.) E-mail: r-nuzzo@illinois.edu.

ORCID

Richard T. Haasch: 0000-0001-9479-2595
Andrew A. Gewirth: 0000-0003-4400-9907

Author Contributions

The manuscript was written through contributions of all authors. All authors have given approval to the final version of the manuscript. L.S. conceived the *operando* Raman, electrochemistry, and SEM experiment; R.T.H. performed XPS measurements; L.S. and R.T.H. contributed on the XPS data analysis.

Notes

The authors declare no competing financial interest.

■ ACKNOWLEDGMENTS

This work was supported as part of the Center for Electrochemical Energy Science, an Energy Frontier Research Center funded by the U.S. Department of Energy (DOE), Office of Science, Basic Energy Sciences (BES). Bruno Giuliano Nicolau, Aaron Petronico, and Maria Chan provided valuable input.

■ REFERENCES

(1) Kamaya, N.; Homma, K.; Yamakawa, Y.; Hirayama, M.; Kanno, R.; Yonemura, M.; Kamiyama, T.; Kato, Y.; Hama, S.; Kawamoto, K.; Mitsui, A. A lithium superionic conductor. *Nat. Mater.* **2011**, *10*, 682−686.

(2) Han, F. D.; Gao, T.; Zhu, Y. J.; Gaskell, K. J.; Wang, C. S. A Battery Made from a Single Material. *Adv. Mater.* **2015**, *27*, 3473−3483.

(3) Tatsumisago, M.; Hayashi, A. Preparation of lithium ion conducting glasses and glass-ceramics for all-solid-state batteries. *J. Non-Cryst. Solids* **2008**, *354*, 1411−1417.

(4) Minami, K.; Hayashi, A.; Tatsumisago, M. Crystallization Process for Superionic Li7P3S11 Glass-Ceramic Electrolytes. *J. Am. Ceram. Soc.* **2011**, *94*, 1779−1783.

(5) Mizuno, F.; Hayashi, A.; Tadanaga, K.; Tatsumisago, M. New, highly ion-conductive crystals precipitated from Li2S-P2S5 glasses. *Adv. Mater.* **2005**, *17*, 918−921.

(6) Seino, Y.; Nakagawa, M.; Senga, M.; Higuchi, H.; Takada, K.; Sasaki, T. Analysis of the structure and degree of crystallisation of 70Li(2)S-30P(2)S(5) glass ceramic. *J. Mater. Chem. A* **2015**, *3*, 2756−2761.

(7) Seino, Y.; Ota, T.; Takada, K.; Hayashi, A.; Tatsumisago, M. A sulphide lithium super ion conductor is superior to liquid ion conductors for use in rechargeable batteries. *Energy Environ. Sci.* **2014**, *7*, 627−631.

(8) Sahu, G.; Lin, Z.; Li, J. C.; Liu, Z. C.; Dudney, N.; Liang, C. D. Air-stable, high-conduction solid electrolytes of arsenic-substituted Li4SnS4. *Energy Environ. Sci.* **2014**, *7*, 1053−1058.

(9) Tominaga, Y.; Yamazaki, K. Fast Li-ion conduction in poly(ethylene carbonate)-based electrolytes and composites filled with TiO2 nanoparticles. *Chem. Commun.* **2014**, *50*, 4448−4450.

(10) Sun, B.; Mindemark, J.; Edstrom, K.; Brandell, D. Polycarbonate-based solid polymer electrolytes for Li-ion batteries. *Solid State Ionics* **2014**, *262*, 738−742.

(11) Teragawa, S.; Aso, K.; Tadanaga, K.; Hayashi, A.; Tatsumisago, M. Formation of Li2S-P2S5 Solid Electrolyte from N-Methylformamide Solution. *Chem. Lett.* **2013**, *42*, 1435−1437.

(12) Teragawa, S.; Aso, K.; Tadanaga, K.; Hayashi, A.; Tatsumisago, M. Preparation of Li2S-P2S5 solid electrolyte from N-methylformamide solution and application for all-solid-state lithium battery. *J. Power Sources* **2014**, *248*, 939−942.

(13) Ito, S.; Nakakita, M.; Aihara, Y.; Uehara, T.; Machida, N. A synthesis of crystalline Li7P3S11 solid electrolyte from 1,2-dimethoxyethane solvent. *J. Power Sources* **2014**, *271*, 342−345.

(14) Yubuchi, S.; Teragawa, S.; Aso, K.; Tadanaga, K.; Hayashi, A.; Tatsumisago, M. Preparation of high lithium-ion conducting Li6PS5Cl solid electrolyte from ethanol solution for all-solid-state lithium batteries. *J. Power Sources* **2015**, *293*, 941−945.

(15) Teragawa, S.; Aso, K.; Tadanaga, K.; Hayashi, A.; Tatsumisago, M. Liquid-phase synthesis of a Li3PS4 solid electrolyte using N-methylformamide for all-solid-state lithium batteries. *J. Mater. Chem. A* **2014**, *2*, 5095−5099.

(16) Kozen, A. C.; Pearse, A. J.; Lin, C. F.; Noked, M.; Rubloff, G. W. Atomic Layer Deposition of the Solid Electrolyte LiPON. *Chem. Mater.* **2015**, *27*, 5324−5331.

(17) Nam, Y. J.; Cho, S. J.; Oh, D. Y.; Lim, J. M.; Kim, S. Y.; Song, J. H.; Lee, Y. G.; Lee, S. Y.; Jung, Y. S. Bendable and Thin Sulfide Solid Electrolyte Film: A New Electrolyte Opportunity for Free-Standing and Stackable High-Energy All-Solid-State Lithium-Ion Batteries. *Nano Lett.* **2015**, *15*, 3317−3323.

(18) Kato, Y.; Hori, S.; Saito, T.; Suzuki, K.; Hirayama, M.; Mitsui, A.; Yonemura, M.; Iba, H.; Kanno, R. High-power all-solid-state batteries using sulfidesuperionic conductors. *Nat. Energy* **2016**, *1*, 16030.

(19) Liu, Z.; Fu, W.; Payzant, E. A.; Yu, X.; Wu, Z.; Dudney, N. J.; Kiggans, J.; Hong, K.; Rondinone, A. J.; Liang, C. Anomalous High Ionic Conductivity of Nanoporous beta-Li3PS4. *J. Am. Chem. Soc.* **2013**, *135*, 975−978.

(20) Hayashi, A.; Tatsumisago, M. Invited Paper: Recent Development of Bulk-Type Solid-State Rechargeable Lithium Batteries with Sulfide Glass-ceramic Electrolytes. *Electron. Mater. Lett.* **2012**, *8*, 199−207.

(21) Takada, K. Progress and prospective of solid-state lithium batteries. *Acta Mater.* **2013**, *61*, 759−770.

(22) Liang, X. M.; Wang, L. Y.; Jiang, Y. M.; Wang, J.; Luo, H.; Liu, C. Y.; Feng, J. W. In-Channel and In-Plane Li Ion Diffusions in the Superionic Conductor Li10GeP2S12 Probed by Solid-State NMR. *Chem. Mater.* **2015**, *27*, 5503−5510.

(23) Weber, D. A.; Senyshyn, A.; Weldert, K. S.; Wenzel, S.; Zhang, W. B.; Kaiser, R.; Berendts, S.; Janek, J.; Zeier, W. G. Structural

DOI: 10.1021/acs.chemmater.7b00034
Chem. Mater. 2017, 29, 3029−3037

Insights and 3D Diffusion Pathways within the Lithium Superionic Conductor Li10GeP2S12. *Chem. Mater.* **2016**, *28*, 5905−5915.
(24) Mo, Y.; Ong, S. P.; Ceder, G. First Principles Study of the Li10GeP2S12 Lithium Super Ionic Conductor Material. *Chem. Mater.* **2012**, *24*, 15−17.
(25) Du, F.; Ren, X.; Yang, J.; Liu, J.; Zhang, W. Structures, Thermodynamics, and Li+ Mobility of Li10GeP2S12: A First-Principles Analysis. *J. Phys. Chem. C* **2014**, *118*, 10590−10595.
(26) Kuhn, A.; Koehler, J.; Lotsch, B. V. Single-crystal X-ray structure analysis of the superionic conductor Li10GeP2S12. *Phys. Chem. Chem. Phys.* **2013**, *15*, 11620−11622.
(27) Gobet, M.; Greenbaum, S.; Sahu, G.; Liang, C. D. Structural Evolution and Li Dynamics in Nanophase Li3PS4 by Solid-State and Pulsed-Field Gradient NMR. *Chem. Mater.* **2014**, *26*, 3558−3564.
(28) Wang, H.; Hood, Z. D.; Xia, Y. N.; Liang, C. D. Fabrication of ultrathin solid electrolyte membranes of beta-Li3PS4 nanoflakes by evaporation-induced self-assembly for all-solid-state batteries. *J. Mater. Chem. A* **2016**, *4*, 8091−8096.
(29) Homma, K.; Yonemura, M.; Kobayashi, T.; Nagao, M.; Hirayama, M.; Kanno, R. Crystal structure and phase transitions of the lithium ionic conductor Li3PS4. *Solid State Ionics* **2011**, *182*, 53−58.
(30) Ohta, N.; Takada, K.; Zhang, L. Q.; Ma, R. Z.; Osada, M.; Sasaki, T. Enhancement of the high-rate capability of solid-state lithium batteries by nanoscale interfacial modification. *Adv. Mater.* **2006**, *18*, 2226−2229.
(31) Takada, K.; Ohta, N.; Zhang, L. Q.; Fukuda, K.; Sakaguchi, I.; Ma, R.; Osada, M.; Sasaki, T. Interfacial modification for high-power solid-state lithium batteries. *Solid State Ionics* **2008**, *179*, 1333−1337.
(32) Richards, W. D.; Miara, L. J.; Wang, Y.; Kim, J. C.; Ceder, G. Interface Stability in Solid-State Batteries. *Chem. Mater.* **2016**, *28*, 266−273.
(33) Zhu, Y. Z.; He, X. F.; Mo, Y. F. First principles study on electrochemical and chemical stability of solid electrolyte-electrode interfaces in all-solid-state Li-ion batteries. *J. Mater. Chem. A* **2016**, *4*, 3253−3266.
(34) Zhu, Y. Z.; He, X. F.; Mo, Y. F. Origin of Outstanding Stability in the Lithium Solid Electrolyte Materials: Insights from Thermodynamic Analyses Based on First-Principles Calculations. *ACS Appl. Mater. Interfaces* **2015**, *7*, 23685−23693.
(35) Adams, S.; Prasada Rao, R. Structural requirements for fast lithium ion migration in Li10GeP2S12. *J. Mater. Chem.* **2012**, *22*, 7687−7691.
(36) Otoyama, M.; Ito, Y.; Hayashi, A.; Tatsumisago, M. Raman imaging for LiCoO2 composite positive electrodes in all-solid-state lithium batteries using Li2S-P2S5 solid electrolytes. *J. Power Sources* **2016**, *302*, 419−425.
(37) Wenzel, S.; Randau, S.; Leichtweiss, T.; Weber, D. A.; Sann, J.; Zeier, W. G.; Janek, J. Direct Observation of the Interfacial Instability of the Fast Ionic Conductor Li10GeP2S12 at the Lithium Metal Anode. *Chem. Mater.* **2016**, *28*, 2400−2407.
(38) Wenzel, S.; Weber, D. A.; Leichtweiss, T.; Busche, M. R.; Sann, J.; Janek, J. Interphase formation and degradation of charge transfer kinetics between a lithium metal anode and highly crystalline Li7P3S11 solid electrolyte. *Solid State Ionics* **2016**, *286*, 24−33.
(39) Wu, H. L.; Huff, L. A.; Gewirth, A. A. In Situ Raman Spectroscopy of Sulfur Speciation in Lithium-Sulfur Batteries. *ACS Appl. Mater. Interfaces* **2015**, *7*, 1709−1719.
(40) Moshkovich, M.; Gofer, Y.; Aurbach, D. Investigation of the electrochemical windows of aprotic alkali metal (Li,Na,K) salt solutions. *J. Electrochem. Soc.* **2001**, *148*, E155−E167.
(41) Esbenshade, J. L.; Gewirth, A. A. Effect of Mn and Cu Addition on Lithiation and SEI Formation on Model Anode Electrodes. *J. Electrochem. Soc.* **2014**, *161*, A513−A518.
(42) Tachez, M.; Malugani, J. P.; Mercier, R.; Robert, G. Ionic-Conductivity of And Phase-Transition in Lithium Thiophosphate Li_3PS_4. *Solid State Ionics* **1984**, *14*, 181−185.
(43) Sourisseau, C.; Cavagnat, R.; Fouassier, M.; Brec, R.; Elder, S. H. Infrared, Raman, Resonance Raman Spectra and Lattice Dynamics Calculations of the Solid Potassium (I) Nickel (II) Thiophosphate Compound, $KNiPS_4$. *Chem. Phys.* **1995**, *195*, 351−369.
(44) Sourisseau, C.; Rodriguez, V.; Jobic, S.; Brec, R. Infrared, Raman and resonance Raman spectra of the solid nickel(II) thiophosphate compound (PPh4)(3) (NiPS4)(3) and force constants in the trinickel Ni3P3S12 (3-) cyclic anion. *J. Raman Spectrosc.* **1999**, *30*, 1087−1097.
(45) Patzmann, U.; Brockner, W.; Cyvin, B. N.; Cyvin, S. J. Darstellung, Oscillation Spectrum and Normal Coordinate Analysis Des Gold Ortho-Thiophosphates, AuPS4. *J. Raman Spectrosc.* **1986**, *17*, 257−261.
(46) Mizuno, F.; Ohtomo, T.; Hayashi, A.; Tadanaga, K.; Tatsumisago, M. Lithium ion conducting solid electrolytes prepared from Li2S, elemental P and S. *Solid State Ionics* **2006**, *177*, 2753−2757.
(47) Hassoun, J.; Verrelli, R.; Reale, P.; Panero, S.; Mariotto, G.; Greenbaum, S.; Scrosati, B. A structural, spectroscopic and electrochemical study of a lithium ion conducting Li10GeP2S12 solid electrolyte. *J. Power Sources* **2013**, *229*, 117−122.
(48) Coste, S.; Bujoli-Doeuff, M.; Louarn, G.; Massiot, D.; Brec, R.; Jobic, S. PPh3-C3H6-PPh3)(0.5) NiPS4 and (PPh3-C2H2-PPh3)(0.5) NiPS4: Two new compounds containing NiPS4 (−) chains. *New J. Chem.* **2003**, *27*, 1228−1232.
(49) Chondroudis, K.; Kanatzidis, M. G.; Sayettat, J.; Jobic, S.; Brec, R. Palladium chemistry in molten alkali metal polychalcophosphate fluxes. Synthesis and characterization of K4Pd(PS4)(2), Cs4Pd(PS4)(2), Cs10Pd(PSe4)(4), KPdPS4, K2PdP2S6, and Cs2PdP2Se6. *Inorg. Chem.* **1997**, *36*, 5859−5868.
(50) Pakiari, A. H.; Jamshidi, Z. Nature and Strength of M-S Bonds (M = Au, Ag, and Cu) in Binary Alloy Gold Clusters. *J. Phys. Chem. A* **2010**, *114*, 9212−9221.
(51) Dietrich, C.; Sadowski, M.; Sicolo, S.; Weber, D. A.; Sedlmaier, S. J.; Weldert, K. S.; Indris, S.; Albe, K.; Janek, J.; Zeier, W. G. Local Structural Investigations, Defect Formation, and Ionic Conductivity of the Lithium Ionic Conductor Li4P2S6. *Chem. Mater.* **2016**, *28*, 8764−8773.
(52) El Jaroudi, O.; Picquenard, E.; Gobeltz, N.; Demortier, A.; Corset, J. Raman spectroscopy study of the reaction between sodium sulfide or disulfide and sulfur: Identity of the species formed in solid and liquid phases. *Inorg. Chem.* **1999**, *38*, 2917−2923.
(53) Lucovsky, G.; deNeufville, J. P.; Galeener, F. L. Study of Optic Modes of $Ge_{0.30}S_{0.70}$ glass by Infrared and Raman Spectroscopy. *Phys. Rev. B* **1974**, *9*, 1591−1597.
(54) Seo, I.; Martin, S. W. Structural Properties of Lithium Thio-Germanate Thin Film Electrolytes Grown by Radio Frequency Sputtering. *Inorg. Chem.* **2011**, *50*, 2143−2150.
(55) Minami, K.; Hayashi, A.; Tatsumisago, M. Preparation and characterization of lithium ion conducting Li2S-P2S5-GeS2 glasses and glass-ceramics. *J. Non-Cryst. Solids* **2010**, *356*, 2666−2669.

DOI: 10.1021/acs.chemmater.7b00034
Chem. Mater. 2017, 29, 3029−3037